Velocity Profile Shapes in Alcator C-Mod Plasmas

J.E. Rice[‡], N.M. Cao[†], A.E. Hubbard[‡] and J.W. Hughes [‡]

[‡]*PSFC MIT, Cambridge, Massachusetts 02139, USA*

[†]*UT, Austin, Texas, 78712 USA*

Abstract

Toroidal rotation velocity spatial profiles (r/a < 0.8) have been obtained from C-Mod over a wide range of operational conditions, including H-mode, I-mode, ICRF-heated L-mode and Ohmic L-mode (LOC and SOC), and in plasmas with ITBs, LH wave injection and MCFD. Peaked, flat and hollow rotation profiles have been observed. In H- and I-mode plasmas, generally with co-current peaked profiles, the peaking is correlated with temperature profile peaking, and both increase with toroidal magnetic field (decrease with ρ_*). Any dependence on density peaking is unclear. For Ohmic L-mode discharges, with LOC, the velocity profiles are usually flat and most often directed co-current, while with SOC the profiles are hollow, mostly co-current at the edge and counter-current in the core. Both of these Ohmic rotation states exist with matched density and temperature profiles (and gradients), indicating that neither gradient is relevant during rotation reversals. For plasmas with LH wave injection and discharges with ITBs, the velocity profiles are hollow while the density and temperature profiles exhibit substantial peaking. Broadly speaking for all operational regimes, there is no unifying ordering of the velocity gradient with plasma parameters.

1. Introduction

It is well established that intrinsic toroidal rotation in tokamak plasmas exhibits a rich phenomenolgy [1] due to the variety of mechanisms at play in different operational regimes. This includes a wide range of velocity profile shapes. Future devices will rely substantially upon instrinsic rotation to provide the benefits of the magnitude and shape of the velocity spatial profile, such as suppression of resistive wall modes and turbulence. Key to this strategy is understanding the mechanisms giving rise to instrinsic rotation in order to exploit it. The focus of this paper is on velocity profile shapes. The toroidal velocity profile evolution is governed by a balance between external torques (momentum sources and sinks) and the momentum flux gradient [2] as

$$m\partial(nv_\phi)/\partial t \;=\; -\nabla\cdot\Gamma_\phi \;+\; S_{\rm ext} \tag{1}$$

where v_ϕ is the toroidal velocity, n is the density, m is the particle mass, Γ_ϕ is the momentum flux and $S_{\rm ext}$ includes external momentum sources and sinks. The toroidal Reynolds stress dominates the momentum flux [3], and consists of three parts:

$$\Gamma_\phi/m \;=\; -\chi_\phi\partial v_\phi/\partial r \;+\; V_p v_\phi \;+\; \Pi^{res} \tag{2}$$

where χ_ϕ is the momentum diffusivity (or viscosity), V_p is the momentum pinch (or convection) and Π^{res} is the residual stress. The importance of the influence of the density gradient operating through the momentum pinch in governing the velocity profile has been emphasized in ASDEX-U plasmas [4]. In this paper, the role of V_p and Π^{res} in the determination of the velocity profile shape in a wide operational range of C-Mod plasmas will be explored.

The experimental setup is described in the next section, followed by a presentation of rotation profile characteristics of H- and I-mode plasmas in section 3, which includes scalings of the velocity profile peaking factor with magnetic field, along with peaking factors for the temperature and density. A similar discussion in a variety of operational regimes is given in section 4, which includes Ohmic L-mode, plasmas with lower hybdrid wave injection, discharges with internal transport barriers and those with mode conversion flow drive. Different parameters and their gradients can dominate in various scenarios. In the last section is a discussion of the results, including the roles of the Coriolis pinch and the residual stress.

2. Experimental Setup

The observations discussed here were obtained from the Alcator C-Mod tokamak, a compact (major radius R = 0.67 m, typical minor radius $a \sim 0.21$ m), high magnetic field ($B_T \leq 8.1$ T) device which had molybdenum plasma facing components [5, 6]. The usual diagnostic complement [7] was available, in addition to 4 MW of ion cyclotron range of frequencies (ICRF) power (with variable frequency), 1.2 MW

of lower hybrid (LH) power at 4.6 GHz [8] and external coils for preventing/inducing locked modes. Multiple operational regimes were available, including linear and saturated Ohmic confinement (LOC and SOC) [9], ICRF heated L-mode [10, 11, 12, 13], H-mode [6] (Ohmic and ICRF heated) and ICRF heated I-mode [14, 15]. Internal transport barriers (ITBs) could be formed with off-axis ICRF wave injection [16] and ICRF mode conversion flow drive (MCFD) was demonstrated [17]. It was also possible to modify the current density profile using LH waves [18].

A large range of plasma parameters was explored from over 200 discharges in the present study: plasma current from 0.4 to 1.7 MA, toroidal magnetic field from 2.5 to 7.9 T, electron density from 0.4 to $4\times10^{20}/\mathrm{m}^3$ and central electron temperature from 0.9 to 6.3 keV. Sawtooth-averaged electron temperature and density spatial profiles were obtained using Thomson scattering [19] and electron temperature profiles from electron cyclotron emission (ECE). Unless otherwise noted, all plasmas were in deuterium. With the exception of occasional ICRF MCFD and LH wave injection, there was no external momentum input and the rotation can be considered instrinsic. Impurity rotation velocity profiles were obtained from a spatially imaging spherical crystal Johann spectrometer system [20, 21] viewing H- and He-like argon ions. Argon was introduced through a piezo-electric valve, resulting in an impurity concentration typically in the range from $10^{-3} - 10^{-4} \times \mathrm{n}_e$. Wavelength calibration was achieved by running locked modes which had 0 rotation across the profile.

3. Velocity Profile Peaking Dependences in H- and I-mode Plasmas

In this section, velocity profile shapes in ICRF heated H- and I-mode plasmas will be explored. H- and I-mode typically exhibit co-current rotation and parameter time histories for a 0.8 MA, 5.4 T H-mode discharge are shown in Fig.1. Of note are that the co-current rotation develops in the outer regions of the plasma before propagating in to the core [22, 23, 24, 25] and that the velocity at the center is about a factor of 2 higher than at the mid-radius during the H-mode phase. Spatial velocity profiles at three different times for this discharge are shown in Fig.2. The target SOC plasma exhibited a hollow shape (to be discussed in the next section), the transition profile indicates that the co-current H-mode rotation developed first at the plasma edge and that during the H-mode phase, the profile was peaked by about a factor of two. Rotation characteristics of I-mode plasmas are very similar to those seen in H-mode [25, 26]. Spatial profiles of for several parameters of interest for a 1.7 MA, 7.8 T I-mode plasma are shown in Fig.3. As was seen in Fig.2, the velocity profile is centrally peaked. Generally speaking, the rotation behavior in H- and I-mode plasmas is identical for all practical purposes. The density and temperature profiles shown are fits to Thomson scattering data [27] and ECE measurements (T_e only).

This velocity profile peaking has been investigated for a database of $\sim$170 H- and I-mode plasmas, covering a range of plasma current from 0.55 to 1.7 MA, magnetic field from 2.7 to 7.9 T and q_{95} from 3.0 to 6.7. In what follows, profile peaking is defined as the ratio of the central value to the value at the mid-radius r/a = 0.5, for the toroidal

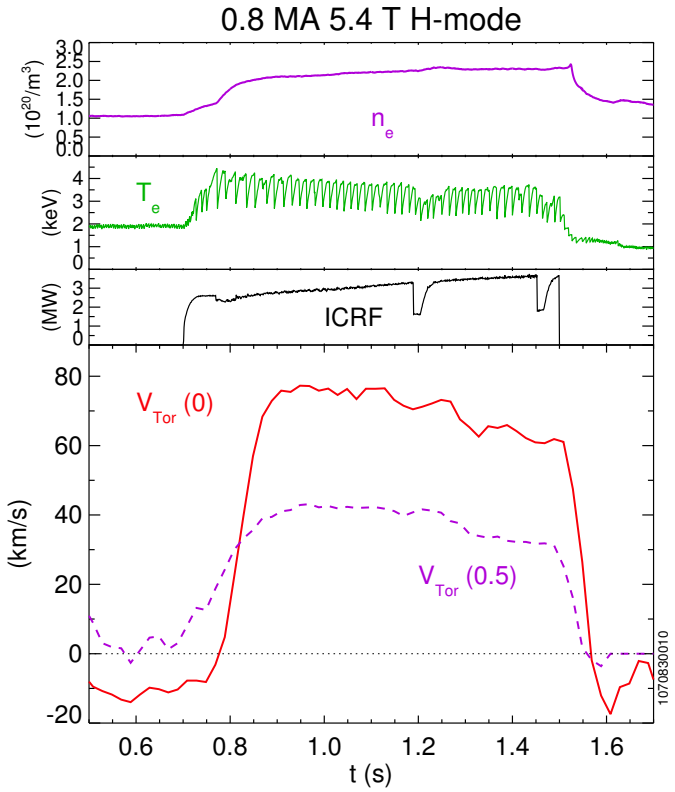

Figure 1: Time histories of the line-average electron density, central electron temperature from ECE, ICRF power and in the bottom frame, the toroidal rotation velocity at the center (solid red line) and at r/a = 0.5 (dashed purple line) for a 0.8 MA, 5.4 T H-mode discharge.

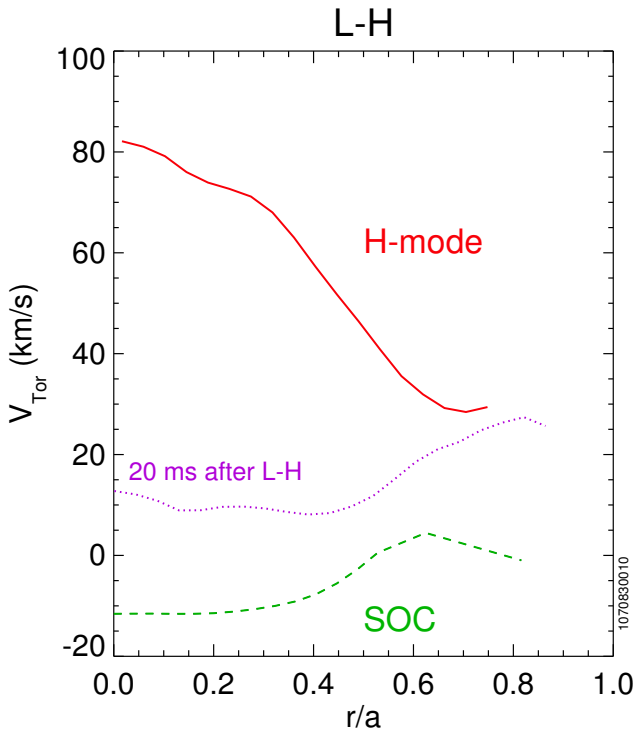

Figure 2: Rotation velocity profiles at three different times for the H-mode discharge of Fig.1: in the SOC phase just before initiation of the ICRF power (green dashed line), 20 ms after the L-H transition (dotted purple line) and after the H-mode was fully developed at 0.91 s (solid red line).

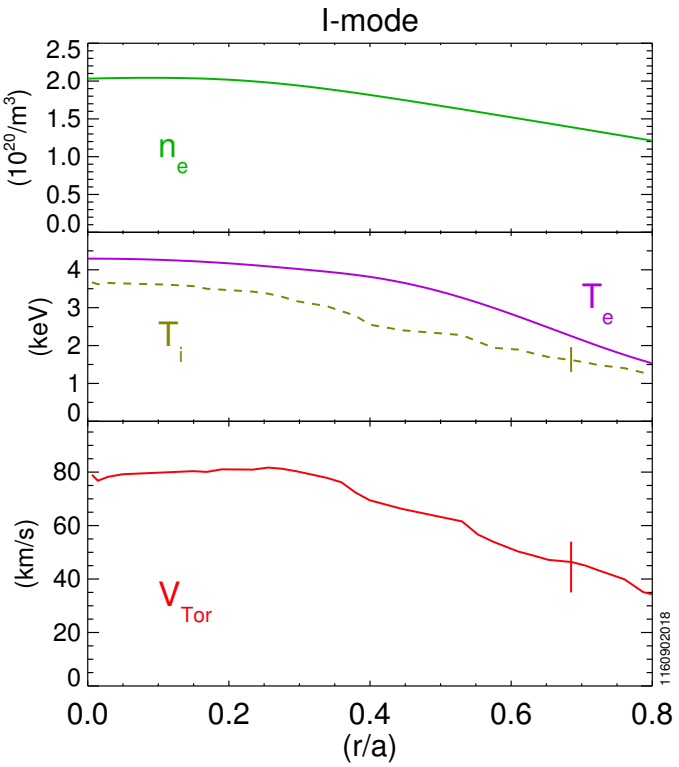

Figure 3: Spatial profiles of the electron density (top), electron and ion temperatures (middle) and rotation velocity (bottom) for a 1.7 MA, 7.8 T I-mode discharge.

velocity, the electron temperature and the electron density. The velocity peaking as a function of toroidal magnetic field for H- and I-mode plasmas is shown in Fig.4. There is a strong correlation between the two, with the velocity peaking increasing as

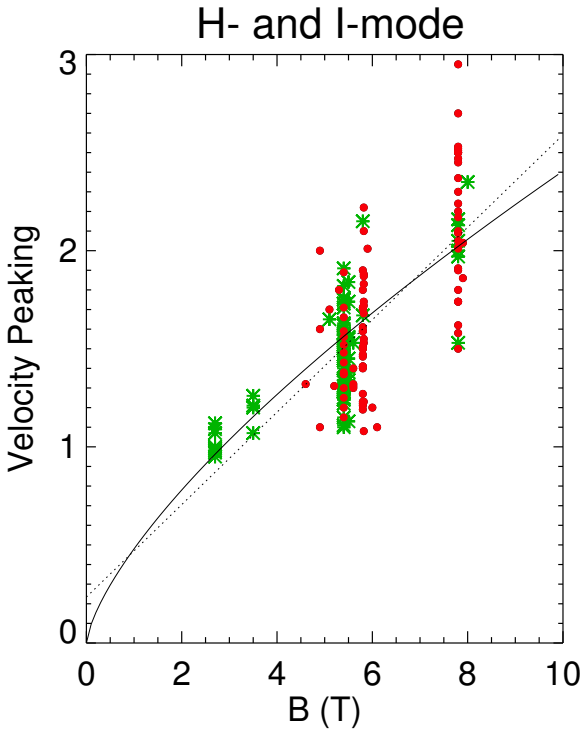

Figure 4: The toroidal velocity peaking factor $V_{Tor}(0)/V_{Tor}(0.5)$ as a function of magnetic field for H- (green asterisks) and I-mode (red dots). The dotted line represents the best linear fit while the solid line is proportional to $B^{0.7}$.

$B^{0.7\pm0.1}$. Note that the H- and I-mode points are well intermixed, except that there are no I-mode points at the lowest magnetic fields, where the I-mode window of operation is small [15]. The question of a dependence on plasma current for this same set of discharges is addressed in Fig.5, where the dependence of the velocity peaking factor $V_{Tor}(0)/V_{Tor}(0.5)$ is shown as a function of q_{95}. There is no apparent dependence of the velocity peaking on q_{95}, which indicates that the plasma current is not the important parameter.

Parameter dependence of electron temperature profile peaking has also been explored for the same set of H- and I-mode discharges. Shown in Fig.6 is the peaking factor $T_e(0)/T_e(0.5)$ as a function of toroidal magnetic field. There is a similar dependence on magnetic field as was seen with the velocity peaking in Fig.4 and the H- and I-mode points are also intermixed. The relation between the velocity and temperature

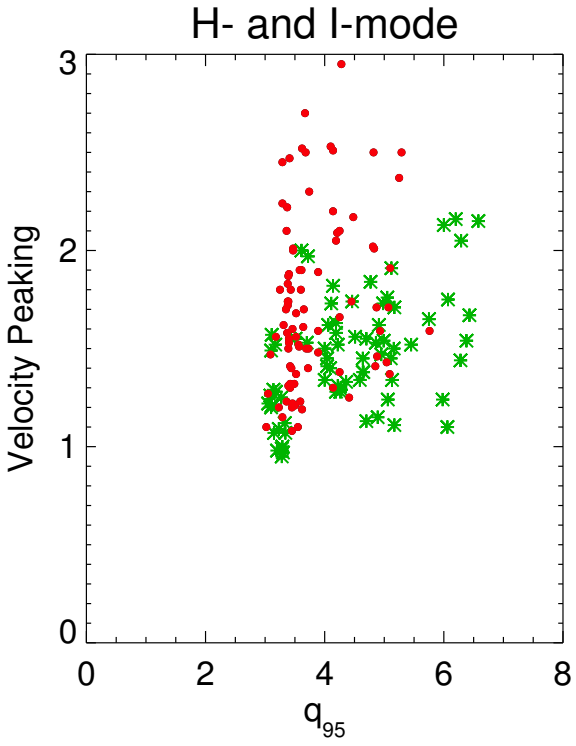

Figure 5: The toroidal velocity peaking factor $V_{Tor}(0)/V_{Tor}(0.5)$ as a function of q_{95} for the same H- (green asterisks) and I-mode (red dots) discharges as shown in Fig.4.

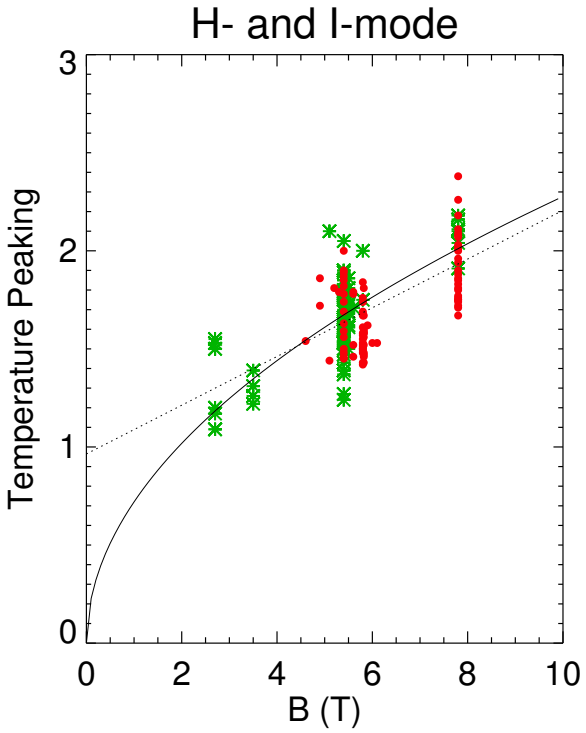

Figure 6: The electron temperature profile peaking factor $T_e(0)/T_e(0.5)$ as a function of magnetic field for H- (green asterisks) and I-mode (red dots) discharges. The dotted line represents the best linear fit while the solid line is proportional to $T^{0.5}$.

peaking factors is demonstrated in Fig.7 in which $V_{Tor}(0)/V_{Tor}(0.5)$ as a function of $T_e(0)/T_e(0.5)$ is shown. There is a strong correlation between velocity and tempera-

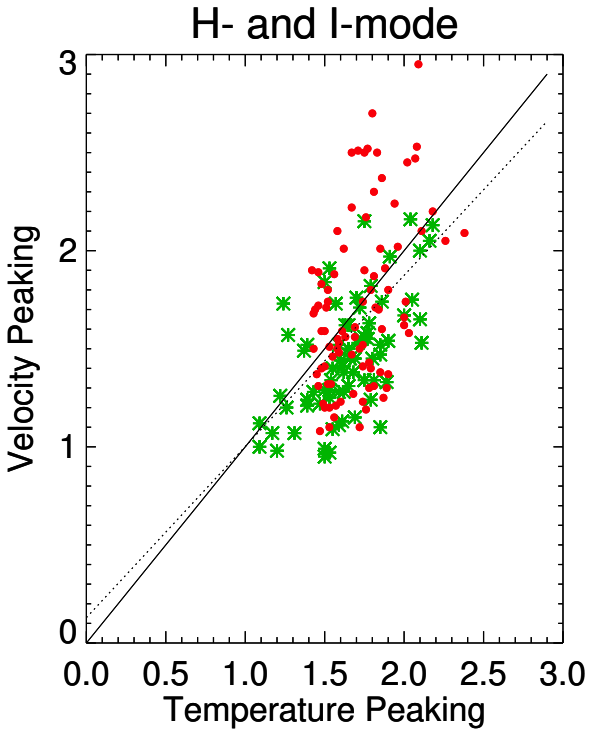

Figure 7: The correlation between velocity and temperature profile peaking in the H- (green asterisks) and I-mode (red dots) discharges from Figs.4 and 6. The dotted line is the best linear fit, while the solid line represents equality.

ture profile peaking for H- and I-mode discharges, with points intermixed, over a large operational range.

A similar exercise has been performed for the electron density profiles on the same set of H- and I-mode discharges. Shown in Fig.8 is the density profile peaking factor $n_e(0)/n_e(0.5)$ as a function of magnetic field. The vertical scale is the same as in Figs.4 and 6 in order to emphasize how comparatively weak the density profile peaking is. In fact, there is barely any dependence on B in H-mode, and the profiles are nearly completely flat. In contrast to the previous cases, there is a different trend between H- and I-mode, with a slight increase in peaking in I-mode, up to a maximum of 1.3. The best linear fits are shown by the lines. It may be the collisionality is the best organizing parameter for the density profile peaking [28, 29]. The correlation between velocity and density profile peaking is shown in Fig.9. There is barely any overlap in the H- and I-mode points, and no variation of the density peaking at all in H-mode. If there is any

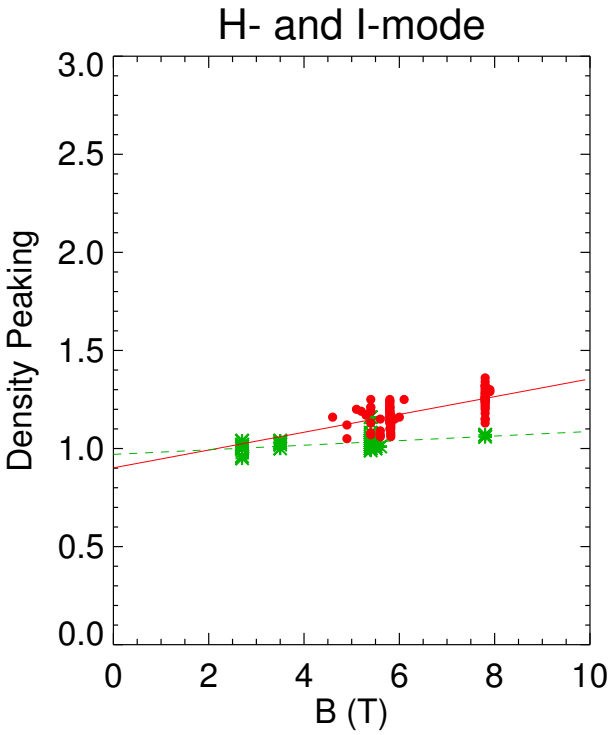

Figure 8: The electron density profile peaking factor $n_e(0)/n_e(0.5)$ as a function of magnetic field for H- (green asterisks) and I-mode (red dots) discharges. The dashed green line represents the best linear fit to the H-mode points while the solid red line is the best linear fit for I-mode.

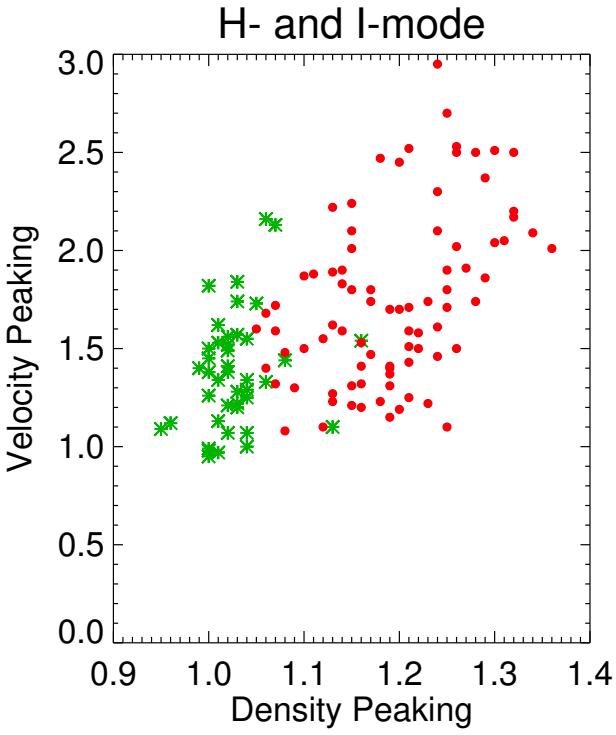

Figure 9: The velocity profile peaking as a function of density profile peaking for H- (green asterisks) and I-mode (red dots) discharges.

dependence of velocity peaking on density peaking in I-mode, it is very weak.

Finally, to demonstrate that sometimes there is no correlation of velocity profile peaking with temperature and density peaking, consider the (atypical) H-mode discharge shown in Fig.10. This unusual plasma, which was formed in the near double

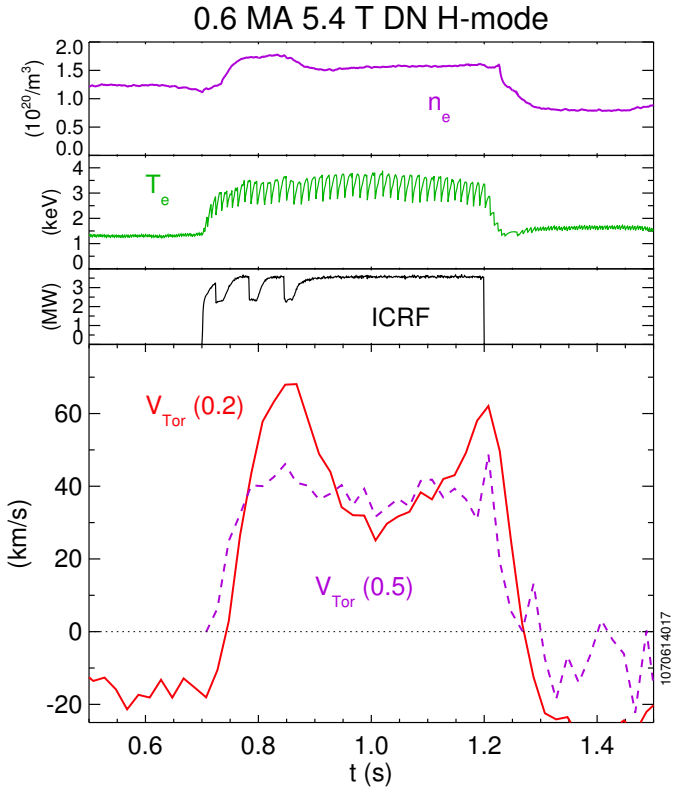

Figure 10: Time histories of the average electron density, central electron temperature, ICRF power and in the bottom frame, the toroidal rotation velocity near the center (solid red line) and at r/a = 0.5 (dashed purple line) for a double null 0.6 MA, 5.4 T H-mode discharge.

null configuration, experienced a substantial drop in the central rotation after the H-mode was established, and then a recovery, while there was very little change at the mid-radius. The cause of this behavior is not known. The relevant profiles for this discharge at two different times are presented in Fig.11. During the hollowing of the velocity profile, there was no measureable change in the density or temperature gradient. The relation between the velocity and temperature peaking shown in Fig.7 is broken here, although a complete correlation is not expected since the temperature cannot change sign, and even a hollowing of the temperature profile would be detrimental to the plasma. And of course in the very edge of enhanced confinement plasmas there is a steep temperature gradient region, whereas at this location there is an E_r well, with

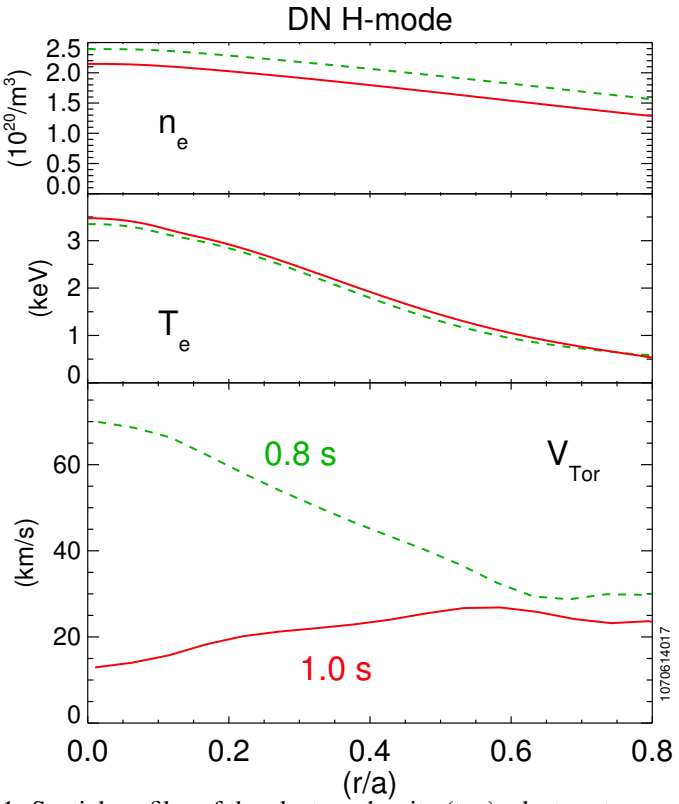

Figure 11: Spatial profiles of the electron density (top), electron temperature (middle) and rotation velocity (bottom) at 0.8 s (green dotted lines) and 1.0 s (solid red lines) for the DN H-mode discharge of Fig.10.

negative toroidal rotation [30], so these two profile shapes are not self-similar.

The results of this section are that in H- and I-mode, there is a stronger correlation between velocity and temperature profile peaking, and that both peaking factors increase with magnetic field. In contrast, the connection between velocity and density profile peaking is weak.

4. Velocity Profile Shapes in Various Operational Scenarios

In the previous section, velocity profile peaking in H- and I-mode plasmas was explored. In this section, velocity profiles under a wide range of operational conditions and scenarios will be examined. A starting point will be basic Ohmic discharges, which can be divided into two distinct categories: low density (low collisionality) LOC plasmas and those at higher density (higher collisionality) with SOC [31, 9]. Both regimes can be produced in a single discharge by means of a density ramp, and an example is shown in Fig.12, which demonstrates a classical core rotation reversal. The transition from the SOC regime (before 0.8 s) to the LOC regime (after 0.9 s) is very sensitive to the decrease in the electron density, and the scale in the top frame is greatly expanded. In the core of the plasma, the rotation was in the counter-current direction with SOC and in the co- direction with LOC. This rotation reversal is a core phenomenon, and there was no change in velocity at r/a = 0.7. Velocity, density and temperature profiles for these two regimes in this discharge are shown in Fig.13. With SOC, the velocity profile is hollow (and counter-current) and with LOC, the profile is relatively flat and directed co-current. These types of profiles are fairly broadly observed [32, 33, 34, 35, 36, 4, 37, 38, 39, 40, 41, 42, 43]. There is no change in the density or temperature gradient near the region of the velocity gradient change, and both co- and counter-current rotation states exist for the same density gradient [35, 42, 43].

The next rotation profiles to be considered are in discharges with LH wave injection, which can impart counter-current torque on the plasma, giving rise to a counter-current change in the intrinsic rotation [44, 45]. Counter-current increments of rotation from the LH waves occur as long as the power level is low enough that the current density profile isn't affected [44, 45, 46, 18, 47, 48, 49, 50]. Shown in Fig.14 are the parameter time histories for a 0.8 MA, 5.4 T discharge with 0.85 MW of LH power injected. The most striking response to the LH waves is the counter-current evolution of the central toroidal rotation. In contrast, there is very little effect at r/a = 0.6, so the net result is a substantial hollowing of the velocity profile in the core plasma. This hollow rotation profile is presented in Fig.15. The hollowing of the co-current velocity profile of the LOC target plasma by the LH waves in the core is apparent, along with a peaking of both the density and temperature profiles [45]. During the LH phase, only Thomson scattering is used for the temperature profile. The correlation between the velocity profile hollowing (peaking in the negative direction) and the density and temperature profile peaking is shown in Fig.16 for several discharges with LH wave injection. For this plot, velocity peaking is defined as the ratio of the change in velocity due to the LH waves (compared to the target plasma) at r/a = 0 and at r/a = 0.5. The reason for using

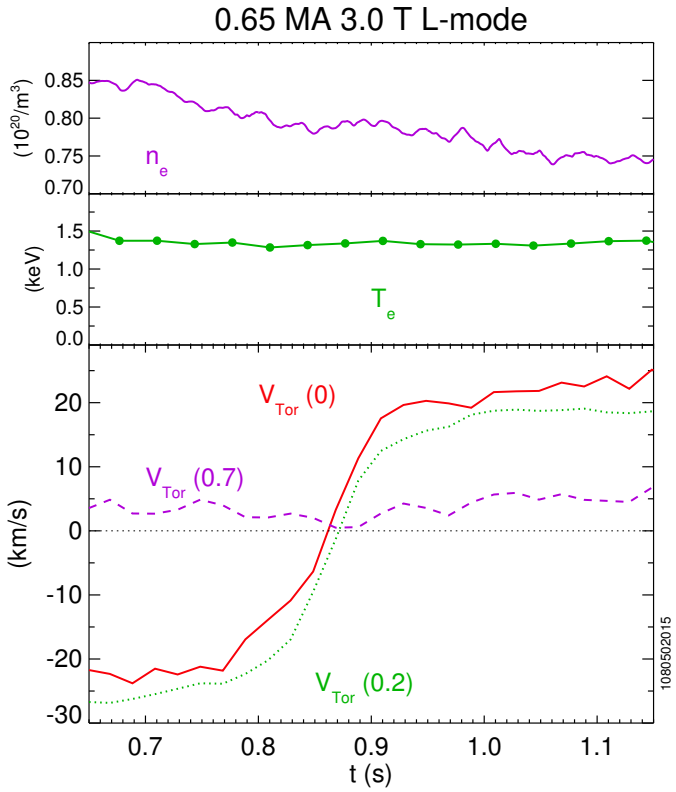

Figure 12: Time histories of the average electron density (top), central electron temperature (middle) and the toroidal rotation velocity at the center (solid red line), at r/a = 0.2 (green dotted line) and at r/a = 0.7 (dashed purple line) for a 0.65 MA, 3.0 T Ohmic L-mode plasma which experienced a core rotation reversal at around 0.85 s.

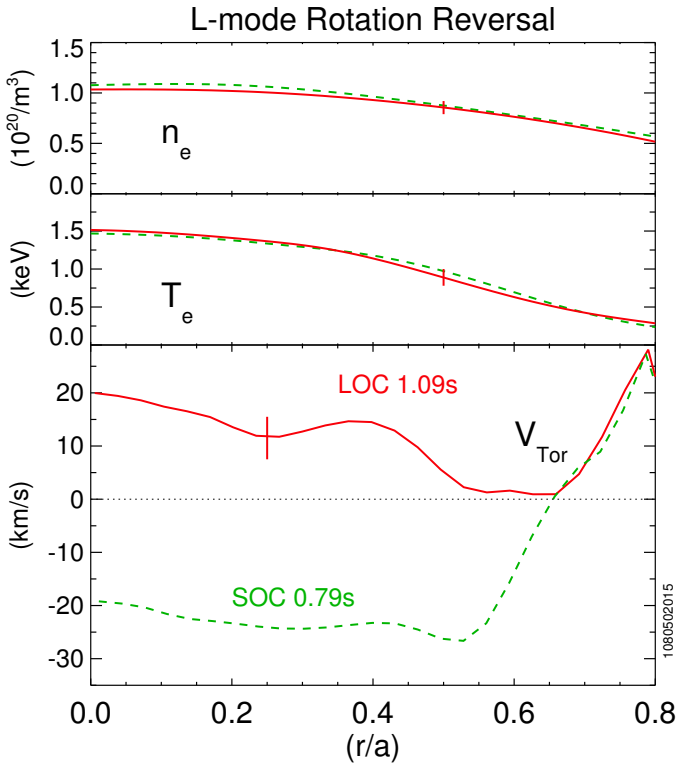

Figure 13: Spatial profiles of the electron density (top), electron temperature (middle) and rotation velocity at 0.79 s (green dashed lines) for the SOC phase and at 1.09 s (solid red lines) for the LOC phase of the rotation reversal discharge of Fig.12. Typical error bars for the density and temperature profiles are shown.

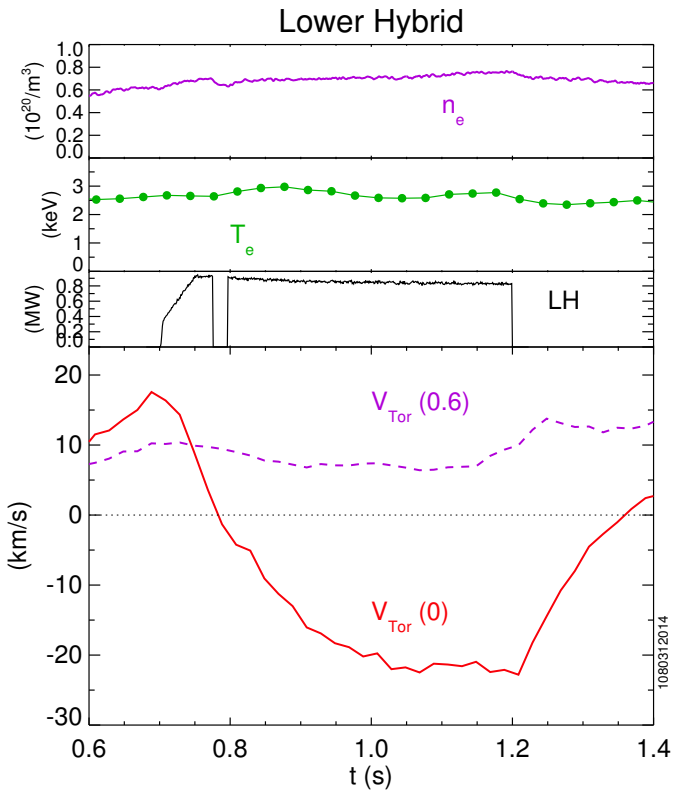

Figure 14: Time histories of the average electron density, central electron temperature, LH power and in the bottom frame, the toroidal rotation velocity at the center (solid red line) and at r/a = 0.6 (dashed purple line) for a 0.8 MA, 5.4 T discharge with LH wave injection (and no ICRF).

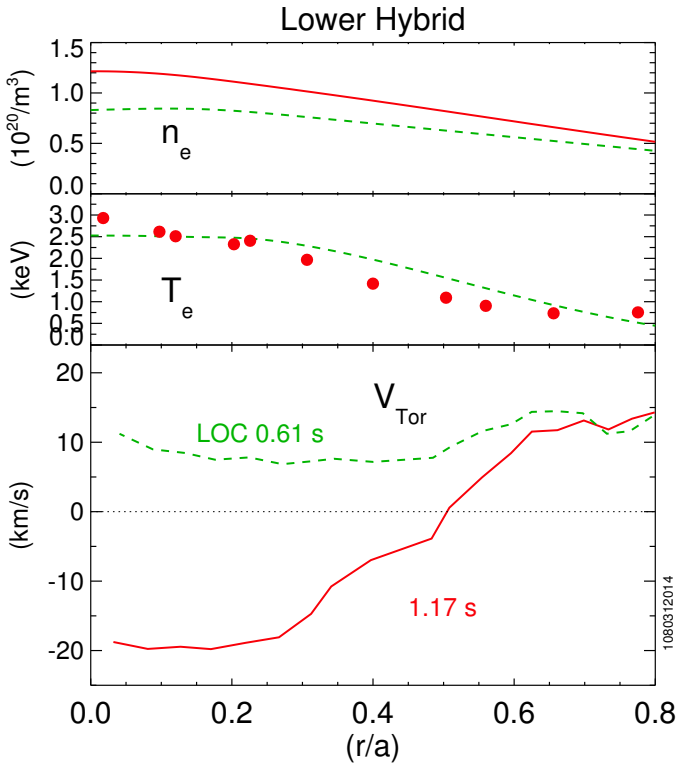

Figure 15: Spatial profiles of the electron density (top), electron temperature (middle) and rotation velocity at 0.61 s (green dashed lines) for the LOC target phase and at 1.17 s (solid red lines and red dots for the temperature) for the LH discharge of Fig.14.

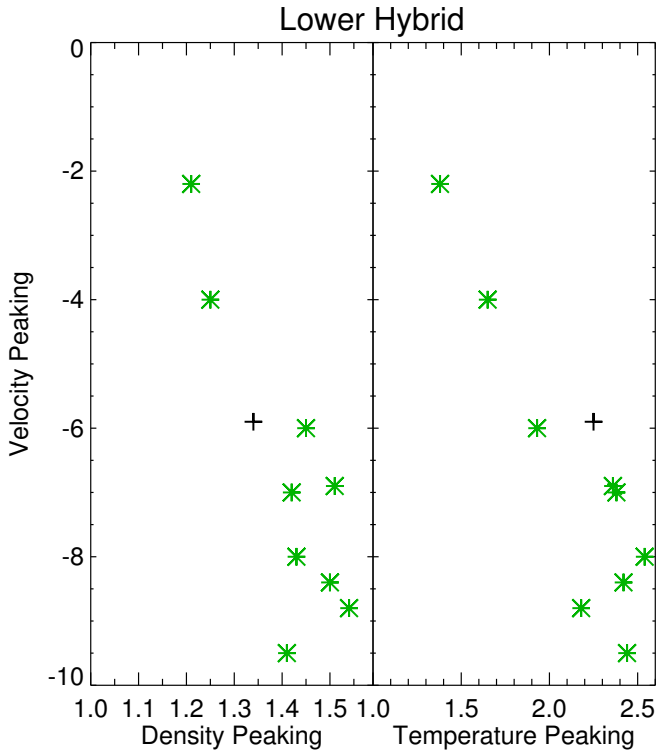

Figure 16: The velocity profile peaking (negative indicates hollowing) as a function of the density profile peaking (left) and the temperature profile peaking (right) for plasmas with LH wave injection. The green asterisks represent the most common case of an L-mode target plasma (both LOC and SOC) while the point indicated by a + sign is from an H-mode target plasma [46].

the change in velocity is that in some cases the velocity hollowing involved going from co- to counter-current values. There is a strong anti-correlation with the density and temperature peaking. This is in contrast to the results of Figs.9 and 7, where there was very weak dependence on density peaking and a strong peaking (rather than hollowing) of the velocity with temperature peaking. It is also noteworthy that the LH plasmas had about a factor of two higher density peaking than was seen in H- and I-mode plasmas. Whether the density profile peaking is a result of the velocity profile hollowing is an open question.

There is another scenario which exhibits a hollowing of the velocity profile in conjunction with strong density peaking: plasmas with ITBs formed by off-axis ICRF heating [51, 16, 52, 22, 23, 53, 54] have hollow velocity profiles and peaked density profiles. A 0.8 MA, 4.6 T ITB plasma time history is shown in Fig.17. The ITB formed

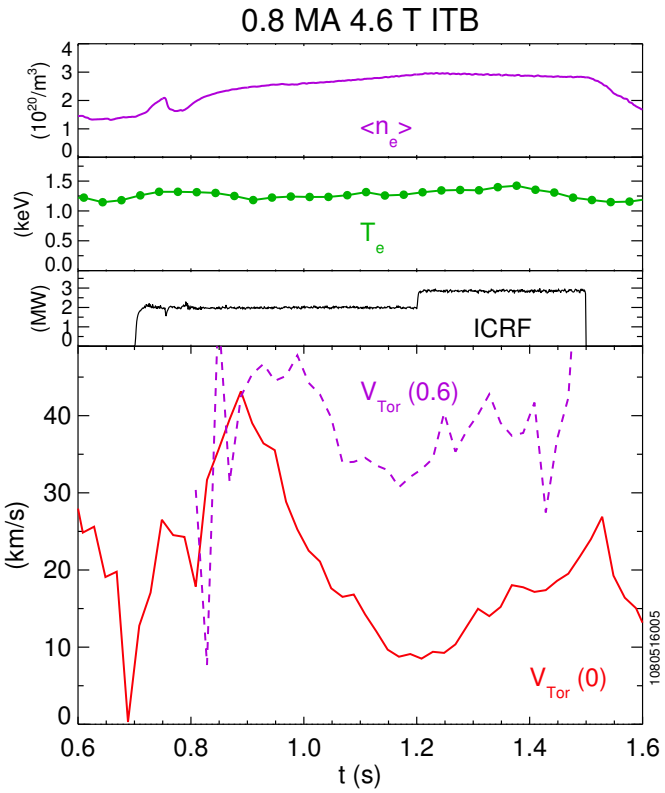

Figure 17: Time histories of the average electron density, central electron temperature, ICRF power and in the bottom frame, the toroidal rotation velocity at the center (solid red line) and at r/a = 0.6 (dashed purple line) for a 0.8 MA, 4.6 T ITB discharge.

just before 0.9 s and was accompanied by a drop in the core rotation and a peaking of the electron density and temperature. At 1.2 s, on-axis heating was added (with the jump in total power, but at a different frequency) which arrested the density increase

and core velocity reduction. The strong hollowing of the velocity profile after the ITB formation is shown in Fig.18. With the ITB formation, there was an extreme hollowing

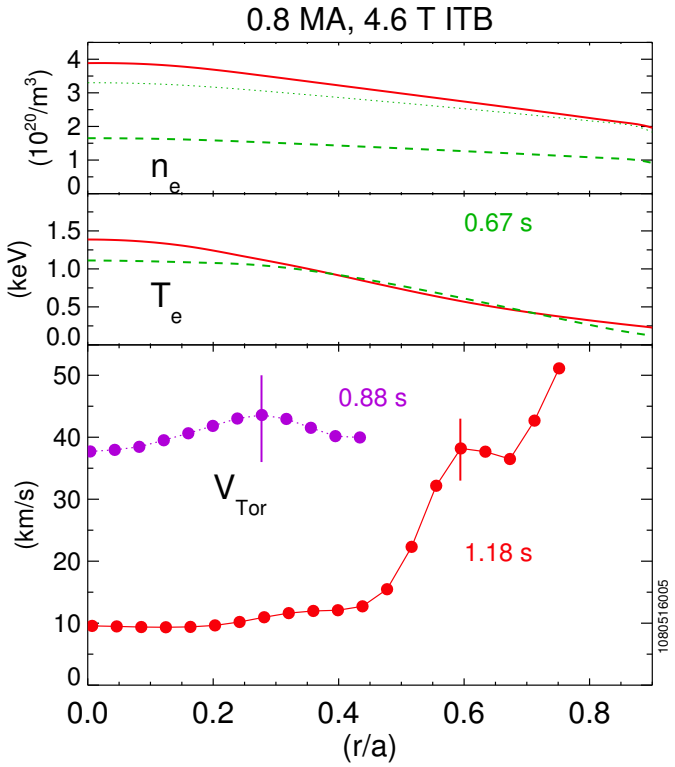

Figure 18: Spatial profiles of the electron density (top) and electron temperature (middle) at 0.67 s (green dashed lines) for the SOC target phase and at 1.18 s (solid red lines) for the ITB discharge of Fig.17. The thin dotted line in the top frame is the 0.67 s profile multiplied by a factor of two to emphasize the density profile peaking. In the bottom frame are the velocity profiles at 0.88 s (H-mode phase as the ITB formed, dotted purple line) and the fully formed ITB phase at 1.18 s (solid red line).

of the velocity profile, in conjunction with a peaking of the density and temperature profiles. With the ITB formation, there is a strong impurity accumulation in the plasma core [16], so the argon level had to be kept low- that is why there is low signal during the pre-ICRF phase and even after the initial H-mode formation, so there is scant velocity profile information before the ITB developed. The very steep velocity gradient between r/a of 0.5 and 0.6 is large enough for the ExB shear suppression to facilitate the ITB formation. The concurrence of hollow velocity profiles with strong density and temperature profile peaking in this case is very similar to that seen with LH wave injection (Figs.14-16).

The final case to be considered involves plasmas with MCFD [17, 55, 56]. Shown

in Fig.19 are the time histories of a 0.8 MA, 5.1 T discharge with MCFD, There is very

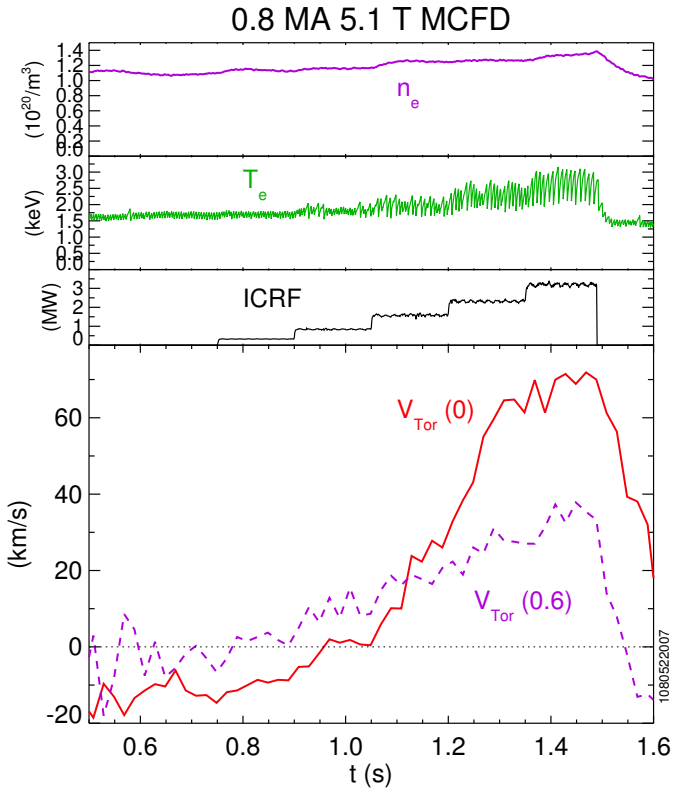

Figure 19: Time histories of the average electron density, central electron temperature, ICRF power and in the bottom frame, the toroidal rotation velocity at the center (solid red line) and at r/a = 0.6 (dashed purple line) for a 0.8 MA, 5.1 T discharge with MCFD.

strong direct rotation drive and substantial velocity peaking compared to the intrinsic rotation profiles in H- and I-mode. This is demonstrated in Fig.20. There is very strong peaking for the rotation profile with this form of external momentum drive, in this case accompanied by strong peaking of the temperature profile, but with very little change in the density gradient.

The results of this section and the previous one indicate that there is no simple, universal ordering or correlation across all operational regimes between the velocity profile shape and those of the density and temperature. This is exemplified in Fig.21 in the case of the density profile shape, where the maximum velocity gradient is plotted against the density gradient at the same location. In addition to all of the cases presented in Figs.1-20, some examples of ICRF heated L-mode are included [12, 13] There is no universal ordering with the density gradient (or R/L_n). A correlation may exist within a given operational scenario, but there is no general unification. The same is true of the temperature gradient. It may be obvious, but the normalized velocity gra-

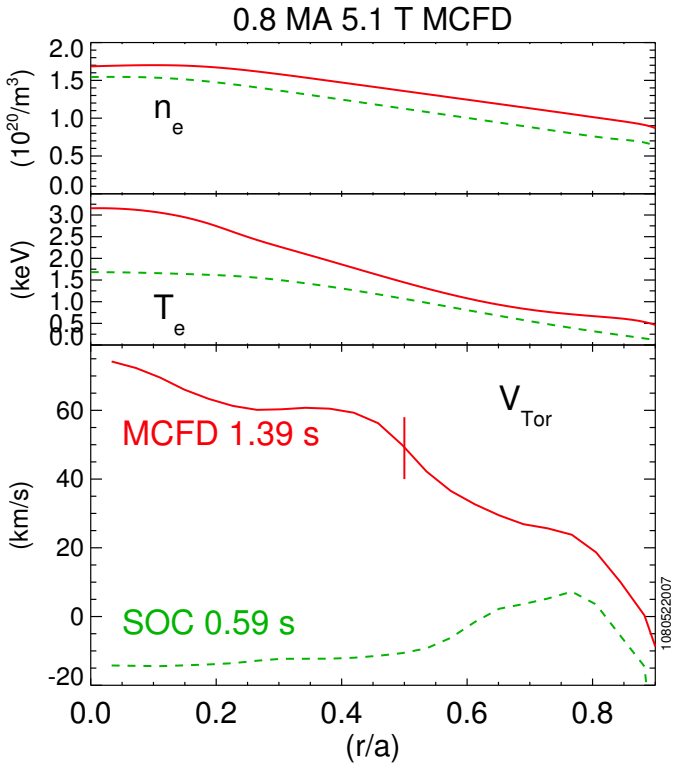

Figure 20: Spatial profiles of the electron density (top), electron temperature (middle) and rotation velocity at 0.59 s (green dashed lines) for the SOC target phase and at 1.39 s (solid red lines) for the MCFD discharge of Fig.19.

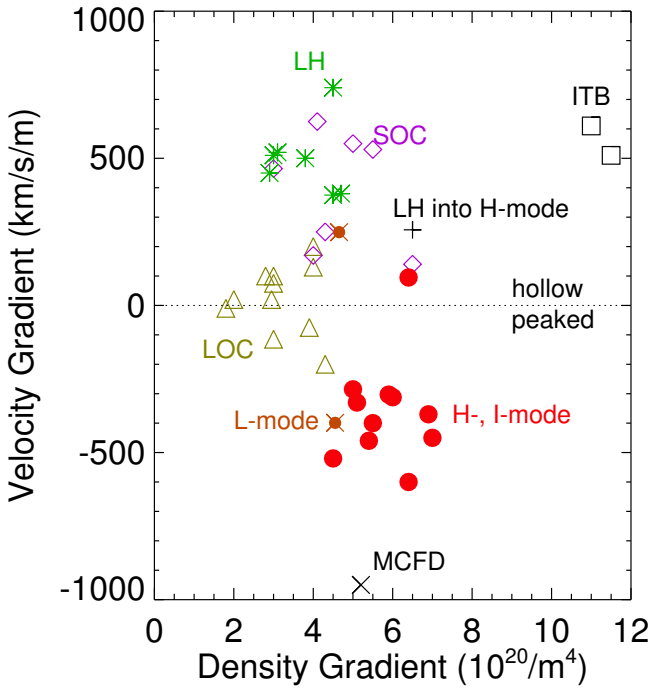

Figure 21: The maximum velocity gradient as a function of the density gradient at the same position for the range of operational regimes covered in this section and the last. Red dots: H- and I-mode; brown triangles: LOC; purple diamonds: SOC; green asterisks: w/LH waves; boxes: ITB plasmas; $\times$: MCFD; orange dot with $\times$: ICRF heated L-mode.

dient scale length R/L$_V$ is a useless ordering parameter, as is demonstrated in Fig.22 for the LH discharge of Fig.15, where the velocity profile passed through the origin, and where there is a singularity. The velocity profile changes sign near the mid-radius,

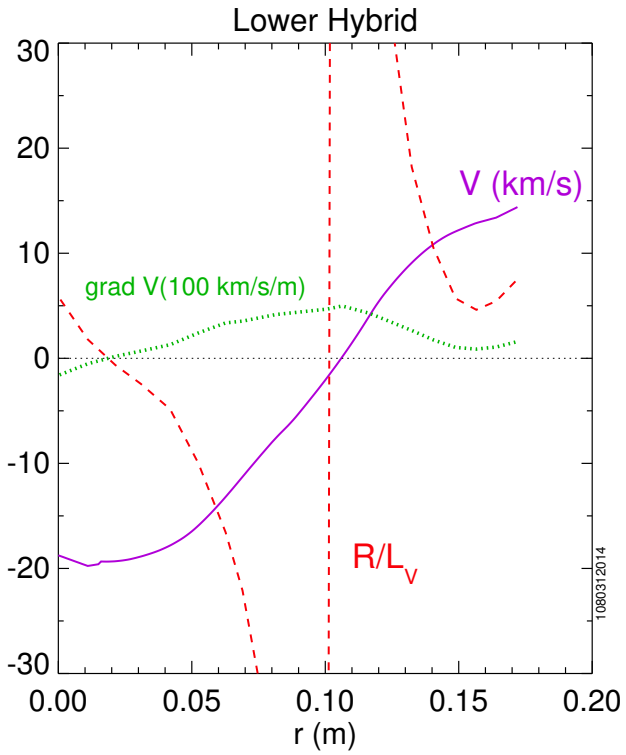

Figure 22: The velocity profile (solid purple line), the velocity gradient (green dotted line) and the normalized velocity gradient scale length R/L$_V$ (dashed red line) for the LH discharge of Fig.15.

close to the maximum of its gradient, and thus the normalized velocity gradient scale length R/L$_V$ exhibits a singularity. Given the unique nature of the velocity, with both positive and negative values observed, the magnitude (and sign) and gradient (and sign) must be treated separately.

5. Discussion

The question arises 'What determines the velocity profile shape?'. Since diffusive momentum transport alone cannot create the observed velocity profiles, it is left to the pinch and the residual stress Π^{res}. The momentum pinch has been treated in depth [57, 58, 59, 60, 61, 3, 62, 63] and can be divided into two general components: the turbulent

equipartition pinch (TEP) and the thermo-electric pinch. With ion temperature gradient (ITG) mode dominance in a fluid treatment, the Coriolis pinch [57] is given by

$$V_p = -\chi_\phi(4 + R/L_n)/R \tag{3}$$

where L_n is the density gradient scale length. There is a correction to this which includes thermo-electric effects [61]

$$V_p = -\chi_\phi(4T_i/T_e + R/L_n)/R \tag{4}$$

due to the electron to ion temperature ratio. In H- and I-mode plasmas, the velocity peaking is only weakly correlated with density profile peaking (see Figs.8 and 9). Furthermore, the density peaking had different trends for H- and I-mode, even though overall velocity profile shapes are the same for both regimes. There was a much stronger correlation with the temperature peaking (Fig.7). This may be related to the fact that the magnitude of the velocity in H- and I-mode has the same dependence on the pedestal temperature gradient [25], and that this occurs due to the temperature gradient dependence of the residual stress [26], with Π^{res} given by [64] (in an ITG mode dominated case)

$$\Pi^{res} = -\rho_* \frac{L_s}{2c_s} \chi_i \left(\frac{\nabla T}{T}\right)^2 v_{thi}^2 \tag{5}$$

where ρ_* is the normalized ion gyroradius, χ_i is the ion thermal conductivity, c_s is the ion sound speed ($\sqrt{T_i/m_i}$) and L_s is the magnetic shear scale length ($R_0 q/\hat{s}$). The implication is that the role of the Coriolis pinch in determination of the velocity profile peaking in H- and I-mode is minimal, whereas the temperature gradient, operating through the residual stress, is key. Regardless of the underlying drive for the velocity profile shape, some information may be buried in the relationship with the magnetic field as was demonstrated in Fig.4. The dependence of the velocity profile peaking on magnetic field may be recast in terms of the normalized gyroradius ρ_*, which is presented in Fig.23. The velocity peaking decreases inversely with ρ_*.

In discharges with LH wave injection, the velocity profile was seen to hollow out (peaking in the counter-current direction) along with substantial peaking of the density and temperature profiles (Fig.16). In these cases, there were similar trends with both the density and temperature peaking, but with a stronger sensitivity to the density peaking. It's interesting to note that the density profile peaking was about a factor of two higher in the LH cases than in H- and I-mode plasmas. A similar trend, velocity profile hollowing with density and temperature peaking, was seen in ITB discharges. An important point here is that LH waves can impart counter-current momentum [49] to the plasma locally where the waves are damped, and this may explain the central hollowing of the velocity profile. It may be that the change in velocity gradient is causing the peaking of the density gradient, rather than the other way around.

The Coriolis pinch cannot change sign unless the density gradient changes from peaked to hollow (or *vice versa*). In the LOC/SOC case of Figs.12 and 13, the rotation

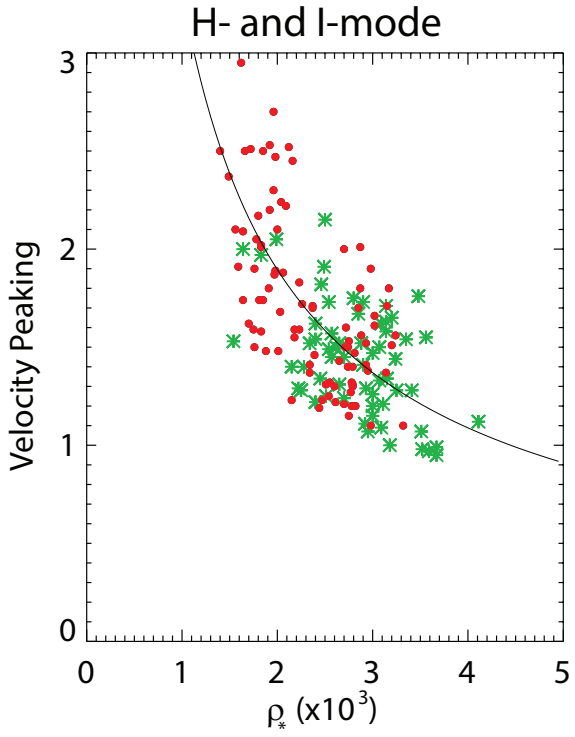

Figure 23: The velocity peaking factor as a function of ρ_* for H- (green asterisks) and I-mode (red dots). The solid line is proportional to ${\rho_*}^{-0.8}$.

Regime	∇n	∇T	other	notes
LOC/SOC	none	none	Π^{res}	both, need sign change
H-/I-mode	weak	linear	$1/\rho_*$	co-
LH	linear	linear	not q(r)	counter-
ITB	linear	linear	E$\times$B	counter-

Table 1: Velocity profile shape dependences for various operational regimes.

reversal (change in sign of the magnitude and gradient of the velocity) cannot be due to the Coriolis pinch since the density gradient remained unchanged. There may be another pinch mechanism at play, but the pinch term in Eq.2 goes to zero when the velocity changes sign, so a pinch process is unlikely. Hence the reversal is probably caused by the residual stress [3], which itself must have changed sign, due to a change of the turbulence propagation direction for example. In fact changes of the dominant turbulent mode dominance accompany the rotation reversal [65], including the propagation direction [66].

Unification of the different velocity profile shape behaviors in terms of a single parameter has not been attained so far, and the dominant mechanism in each operational regime should be treated independently. A summary of the velocity profile shape dependences from various operational regimes is shown in Table 1. The first column gives the operational regime, columns 2-4 indicate dependences on ∇n, ∇T and other, repectively. The last column denotes the rotation direction. The main takeaway here is that the role of the density gradient in the momentum pinch is not always the dominant factor in the determination of the velocity profile shape, that anomalous pinch mechanism(s) may be at play and that further study of the parameter dependence of the residual stress in various operational regimes is necessary. It's also important to recognize that this is a chicken-egg problem and it might be that the rotation profile is influencing the density and temperature profiles, rather than the other way around.

What is the outlook for predicting velocity peaking/∇v in future devices? In H- and I-mode, the co-current velocity profile shape mimics the temperature profile, with a connection to the density profile less clear. If peaked rotation profiles are of interest, peaking decreases with increasing ρ_*, so this bodes well for future high magnetic field machines. Understanding Π^{res} is essential for understanding of the velocity profile.

5. Acknowledgements

The authors thank C. Gao, M. Greenwald, A. Ince-Cushman, J. Irby, Y. Lin, E. Marmar, Y. Podpaly, M. Reinke, G. Wallace, S. Wolfe, S. Wukitch and the entire C-Mod team for expert operation of the device. Work supported at MIT by DoE Award DE-SC0014264.

References

[1] Rice J.E., 2022 "Driven rotation, self-generated flow, and momentum transport in tokamak plasmas", Springer Series on Atomic, Optical, and Plasmas Physics **119**, ISBN 978-3-030-92265-8.

[2] Ida K. and Rice J.E., 2014 *Nucl. Fusion* **54** 045001.

[3] Diamond P.H. *et al.*, 2009 *Nucl. Fusion* **49** 045002.

[4] McDermott R.M. *et al.*, 2014 *Nucl. Fusion* **54** 043009.

[5] Marmar E.S. *et al.*, 2007 *Fusion Sci. Technol.* **51** 261.

[6] Greenwald M. *et al.*, 2014 *Phys. Plasmas* **21** 110501.

[7] Basse N.P. *et al.*, 2007 *Fusion Sci. Technol.* **51** 476.

[8] Bonoli P.T. *et al.*, 2007 *Fusion Sci. Technol.* **51** 401.

[9] Rice J.E. *et al.*, 2020 *Nucl. Fusion* **60** 105001.

[10] Rice J.E. *et al.*, 1998 *Nucl. Fusion* **38** 75.

[11] Rice J.E. *et al.*, 1999 *Nucl. Fusion* **39** 1175.

[12] Reinke M. *et al.*, 2013 *Plasma Phys. Control. Fusion* **55** 012001.

[13] Chilenski M.A. *et al.*, 2017 *Nucl. Fusion* **57** 126013.

[14] Whyte D.G. *et al.*, 2010 *Nucl. Fusion* **50** 105005.

[15] Hubbard A.E. *et al.*, 2016 *Nucl. Fusion* **56** 086003.

[16] Rice J.E. *et al.*, 2002 *Nucl. Fusion* **42** 510.

[17] Lin Y. *et al.*, 2008 *Phys. Rev. Lett.* **101** 235002.

[18] Rice J.E. *et al.*, 2013 *Phys. Rev. Lett.* **111** 125003.

[19] Hughes J.W. *et al.*, 2003 *Rev. Sci. Instrum.* **74** 1667.

[20] Ince-Cushman A. *et al.*, 2008 *Rev. Sci. Instrum.* **79** 10E302.

[21] Reinke M.L. *et al.*, 2012 *Rev. Sci. Instrum.* **83** 113504.

[22] Lee W.D. *et al.*, 2003 *Phys. Rev. Lett.* **91** 205003.

[23] Rice J.E. *et al.*, 2004 *Nucl. Fusion* **44** 379.

[24] Rice J.E. *et al.*, 2004 *Phys. Plasmas* **11** 2427.

[25] Rice J.E. *et al.*, 2011 *Phys. Rev. Lett.* **106** 215001.

[26] Rice J.E. *et al.*, 2017 *Nucl. Fusion* **57** 116004.

[27] Ma Y, 2012 “Study of H-mode Access Conditions on the Alcator C-Mod Tokamak”, Ph.D. dissertation Massachusetts Institute of Technology.

[28] Angioni C. *et al.*, 2007 *Nucl. Fusion* **47** 1326.

[29] Greenwald M. *et al.*, 2007 *Nucl. Fusion* **47** L26.

[30] McDermott R. *et al.*, 2009 *Phys. Plasmas* **16** 056103.

[31] Rice J.E. *et al.*, 2012 *Phys. Plasmas* **19** 056106.

[32] Bortolon A. *et al.*, 2006 *Phys. Rev. Lett.* **97** 235003.

[33] Duval B.P. *et al.*, 2007 *Plasma Phys. Control. Fusion* **49** B195.

[34] Duval B.P. *et al.*, 2008 *Phys. Plasmas* **15** 056113.

[35] Rice J.E. *et al.*, 2011 *Nucl. Fusion* **51** 083005.

[36] Rice J.E. *et al.*, 2013 *Nucl. Fusion* **53** 033004.

[37] Hillesheim J.C. *et al.*, 2015 *Nucl. Fusion* **55** 032003.

[38] Na D.H. *et al.*, 2016 *Nucl. Fusion* **56** 036001.

[39] Camenen Y. *et al.*, 2017 *Plasma Phys. Control. Fusion* **59** 034001.

[40] Na D.H. *et al.*, 2017 *Nucl. Fusion* **57** 126008.

[41] Grierson B.A. *et al.*, 2019 *Phys. Plasmas* **26** 042304.

[42] Cao N.M. *et al.*, 2019 *Nucl. Fusion* **59** 104001.

[43] Cao N.M. *et al.*, 2020 *Phys. Plasmas* **27** 052303.

[44] Ince-Cushman A. *et al.*, 2009 *Phys. Rev. Lett.* **102** 035002.

[45] Rice J.E. *et al.*, 2009 *Nucl. Fusion* **49** 025004.

[46] Rice J.E. *et al.*, 2013 *Nucl. Fusion* **53** 093015.

[47] Chouli B. *et al.*, 2014 *Plasma Phys. Control. Fusion* **56** 095018.

[48] Chouli B. *et al.*, 2015 *Plasma Phys. Control. Fusion* **57** 125007.

[49] Rice J.E. *et al.*, 2016 *Nucl. Fusion* **56** 036015.

[50] Nave M.F.F. *et al.*, 2017 *Nucl. Fusion* **57** 034002.

[51] Rice J.E. *et al.*, 2001 *Nucl. Fusion* **41** 277.

[52] Rice J.E. *et al.*, 2003 *Nucl. Fusion* **43** 781.

[53] Rice J.E. *et al.*, 2008 *Plasma Phys. Control. Fusion* **50** 124042.

[54] Fiore C.L. *et al.*, 2010 *Nucl. Fusion* **50** 064008.

[55] Lin Y. *et al.*, 2009 *Phys. Plasmas* **16** 056102.

[56] Lin Y. *et al.*, 2011 *Nucl. Fusion* **51** 063002.

[57] Peeters A.G. *et al.*, 2007 *Phys. Rev. Lett.* **98** 265003.

[58] Hahm T.S. *et al.*, 2007 *Phys. Plasmas* **14** 072302.

[59] Hahm T.S. *et al.*, 2008 *Phys. Plasmas* **15** 055902.

[60] Gurcan O.D. *et al.*, 2008 *Phys. Rev. Lett.* **100** 135001.

[61] Peeters A.G. *et al.*, 2009 *Phys. Plasmas* **16** 034703.

[62] Peeters A.G. *et al.*, 2011 *Nucl. Fusion* **51** 094027.

[63] Angioni C. *et al.*, 2012 *Nucl. Fusion* **52** 114003..

[64] Kosuga Y. *et al.*, 2010 *Phys. Plasmas* **17** 102313.

[65] Rice J.E. *et al.*, 2011 *Phys. Rev. Lett.* **107** 265001.

[66] Conway G.D. *et al.*, 2006 *Nucl. Fusion* **46** S799.